# The Influence of Vegetation on the Development and Structure of Mountain Waves

ROMUALDO ROMERO AND SERGIO ALONSO

*Group of Geophysical Fluid Dynamics, Departament de Física, Universitat de les Illes Balears, Palma de Mallorca, Spain*

EVERETT C. NICKERSON

*NOAA/FSL, Boulder, Colorado*

CLEMENTE RAMIS

*Group of Geophysical Fluid Dynamics, Departament de Física, Universitat de les Illes Balears, Palma de Mallorca, Spain*

(Manuscript received 23 September 1994, in final form 6 March 1995)

ABSTRACT

The influence of vegetative cover on the development of mountain waves is analyzed using a two-dimensional meso-$\beta$ model. The model includes a detailed representation of surface fluxes and friction that evolve in time as the incoming solar radiation interacts with the soil and vegetation. Simulations of a zonal flow over a north–south-oriented ridge covered by different types of vegetation are presented and examined. The intensity of downslope winds and turbulent kinetic energy structure appear to be especially sensitive to the presence and type of vegetation. Model-predicted rainfall is also examined, indicating an enhancement when mountainous areas are covered by conifer forest.

## 1. Introduction

In recent years, studies have been carried out dealing with the influence of soil and vegetative characteristics on the development of mesoscale circulations. These studies have emphasized the important role played by soil texture through its influence on surface moisture availability, but have indicated that for soils with an adequate water supply, sufficiently dense vegetative cover becomes the dominant surface factor in the evolution of the planetary boundary layer (PBL) (Pinty et al. 1989). However, soil properties must be taken into account in cases of sparse vegetation or when the soil is subjected to a water deficit. To isolate the effects of such surface inhomogeneities, those simulations have emphasized the simplest conditions: flat terrain, clear-sky situations, and/or an unperturbed synoptic environment. With those conditions, thermally induced circulations such as sea breezes or circulations associated with differential heating between zones of different soil or vegetative properties have been simulated (Mahfouf et al. 1987; Pinty et al. 1989).

On the other hand, idealized or real cases of flows over complex terrain have been used in numerical models to describe atmospheric perturbations induced by orography. Simulations with simplified orography and atmospheres of linear and nonlinear flows over mountains have extended the theoretical concepts of mountain waves and have proved useful in testing the correctness and sensitivity of the model approach (e.g., Klemp and Lilly 1978; Anthes and Warner 1978; Mahrer and Pielke 1978; Nickerson et al. 1986). Successful simulations of the well-documented 11 January 1972 windstorm in Boulder, Colorado, have been carried out (e.g., Klemp and Lilly 1978; Durran and Klemp 1983) and have indicated that the inclusion of surface frictional effects gives a more realistic development and evolution of downslope winds (Richard et al. 1989). The damping effects of atmospheric water vapor and liquid water on the development of mountain waves have also been considered (Durran and Klemp 1983); however, sensitivity studies have not been presented that demonstrate the response of mountain waves to different specifications of surface properties.

In the present paper, 2D numerical experiments are carried out using a meso-$\beta$ model with a detailed representation of the soil–atmosphere interface to study the effects of different vegetative covers on the dynamical and thermodynamical structure of atmospheric waves induced by a bell-shaped ridge. Surface fluxes and model-predicted rainfall are also examined.

This paper contains a brief description of the model (section 2). Section 3 presents the particular

*Corresponding author address:* Dr. Clemente Ramis, Group of Geophysical Fluid Dynamics, Departament de Física, Universitat de les Illes Balears, Facultat de Ciencies, 07017 Palma, Spain.
E-mail: dfscrn0@ps.uib.es

conditions for the individual experiments. Results of the simulations including the wave structure, an examination of different terms composing the energy balance at the surface, as well as an examination of the surface pressure drag and the model-predicted rainfall are presented in section 4. Section 5 contains the conclusions.

## 2. Model description

The simulations were done using a hydrostatic meso-$\beta$ model with parameterized microphysics (Nickerson et al. 1986). Model equations are expressed in a terrain-following coordinate system, where the vertical coordinate $\nu$ is related to the usual $\sigma$ coordinate by the expression

$$\sigma = \frac{1}{3}(4\nu - \nu^4).$$

The $\nu$ coordinate provides for high vertical resolution within the PBL, while at the same time preserving equal spacing between the computational levels.

In the atmospheric domain, the vertical and horizontal grids are staggered. Centered differences are used to represent the time and space derivatives. However, an Asselin filter is applied to connect odd and even time steps. The filtered value at the $t - 1$ time level $\tilde{\chi}^{t-1}$ is given by

$$\tilde{\chi}^{t-1} = \chi^t + \alpha(\chi^{t+1} - 2\chi^t + \chi^{t-1}),$$

where the coefficient $\alpha$ takes a value of 0.25 (Schlesinger et al. 1983).

The governing equations are summarized below (the discretized version can be found in Nickerson and Magaziner 1976).

### a. Dynamical equations

The prognostic equation for the horizontal momentum variable (see appendix for symbols), after neglecting the Coriolis term, has the form

$$\frac{\partial \pi u}{\partial t} = -\frac{\partial \pi u u}{\partial x} - \frac{1}{\sigma'}\frac{\partial \sigma' \pi u \dot{\nu}}{\partial \nu} + \left(\phi - \frac{R_v T^* \sigma \pi}{P}\right)\frac{\partial \pi}{\partial x} - \frac{\partial \pi \phi}{\partial x} + F_{\pi u} + D_{\pi u}. \quad (1)$$

The vertical velocity $\dot{\nu}$ is given by

$$\dot{\nu} = -\frac{1}{\pi \sigma'}\int_0^{\nu} \sigma'\left(\frac{\partial \pi}{\partial t} + \frac{\partial \pi u}{\partial x}\right)d\nu. \quad (2)$$

The vertical integration of the continuity equation gives the temporal evolution of the surface pressure:

$$\frac{\partial \pi}{\partial t} = -\int_0^1 \frac{\partial \pi u}{\partial x}\sigma' d\nu, \quad (3)$$

and the geopotential $\phi$ is calculated from the equation

$$\frac{\partial \phi}{\partial \tilde{P}} = -C_p\theta(1 + 0.61q_v). \quad (4)$$

### b. Thermodynamical equations

An entropy variable $S = \pi H$ is defined by

$$H = \ln\left(\frac{T}{\tilde{P}}\right) + \frac{L_v q_v}{C_p T},$$

which is approximately conserved in a pseudoadiabatic, pseudoreversible system. The other predicted thermodynamic variable is $W = \pi(q_v + q_{cw})$, which takes into account the transformation between $q_v$ and $q_{cw}$ when saturation occurs:

$$\frac{\partial S}{\partial t} = -\frac{\partial S u}{\partial x} - \frac{1}{\sigma'}\frac{\partial \sigma' S \dot{\nu}}{\partial \nu} + F_S + D_S + S_S \quad (5)$$

$$\frac{\partial W}{\partial t} = -\frac{\partial W u}{\partial x} - \frac{1}{\sigma'}\frac{\partial \sigma' W \dot{\nu}}{\partial \nu} + F_W + D_W + S_W. \quad (6)$$

The source–sink terms $S_S$ and $S_W$ will contain, respectively, radiative processes (short- and longwave) and transformations between rainwater and the moisture variable $W$ (loss by autoconversion and accretion, and production by evaporation).

### c. Microphysical equations

Separate prognostic equations are written for both rainwater mixing ratio and raindrop number concentration:

$$\frac{\partial \pi q_r}{\partial t} = -\frac{\partial \pi q_r u}{\partial x} - \frac{1}{\sigma'}\frac{\partial \sigma' \pi q_r \dot{\nu}}{\partial \nu} + F_{\pi q_r} + D_{\pi q_r} + S_{\pi q_r} \quad (7)$$

$$\frac{\partial \pi N_r}{\partial t} = -\frac{\partial \pi N_r u}{\partial x} - \frac{1}{\sigma'}\frac{\partial \sigma' \pi N_r \dot{\nu}}{\partial \nu} + F_{\pi N_r} + D_{\pi N_r} + S_{\pi N_r}. \quad (8)$$

The terms $S_{\pi q_r}$ and $S_{\pi N_r}$ are related to autoconversion, self-collection, accretion, evaporation, and sedimentation processes. However, self-collection affects only the concentration of raindrops, whereas accretion affects only the rainwater mixing ratio. Detailed explanation of each partial contribution, based on a log-normal raindrop distribution, are in Nickerson et al. (1986).

### d. Mixing terms and TKE equation

In the model equations, the terms noted as $D_{\text{var}}$(var $= \pi u$, $S$, $W$, etc.) represent horizontal diffusion, which is numerically introduced by a fourth-order operator that is more selective than a second-order one. On the other hand, the $F_{\text{var}}$ terms represent the vertical tur-

bulent mixing and are parameterized according to an eddy coefficient $K_{ex}$:

$$F_{var} = B\frac{\partial}{\partial \nu}\left(BK_{ex}\frac{\partial var}{\partial \nu}\right)$$

with

$$B = -\frac{gP}{\pi R_v T\sigma'}.$$

The exchange coefficients $K_{ex}$ [$K_m$ for the momentum, $K_\theta$ for the thermodynamic and microphysical variables, and $K_e$ for the turbulent kinetic energy (TKE)] are calculated as functions of the TKE and the mixing length $l_k$ following Therry and Lacarrère (1983). The TKE is given by the equation

$$\frac{\partial \pi e}{\partial t} = -\frac{\partial \pi e u}{\partial x} - \frac{1}{\sigma'}\frac{\partial \sigma' \pi e \dot{\nu}}{\partial \nu} + \pi K_m\left(B\frac{\partial u}{\partial \nu}\right)^2 - \frac{g}{\theta_v}\pi K_\theta B\left(\frac{\partial \theta_v}{\partial \nu} - \gamma_{cg}\right) - C_\epsilon \pi\frac{e^{3/2}}{l_\epsilon} + F_{\pi e} + D_{\pi e}. \quad (9)$$

Generalized specifications for $l_k$ and the dissipation length $l_\epsilon$, based on the resistance to vertical displacements due to the static stability, are used by the model following Bougeault and Lacarrère (1989), which parameterization gives a good response outside the PBL.

### e. Upper and lower boundary conditions

At the top of the model, the vertical velocity $\dot{\nu}$ is set to zero. To minimize reflection from the upper boundary, an absorbing layer is included in which the background diffusion (imposed by a second-order operator in this layer) is progressively increased, reaching its maximum value at the uppermost level.

The energy and water budget equations are solved at the air–soil interface to obtain the temperature and moisture at the surface. As explained in Mahfouf et al. (1987) and Pinty et al. (1989), vertical diffusion equations for temperature $T_s$ and volumetric water content $\eta$ are solved in the multilayer soil following McCumber and Pielke (1981):

$$\rho c\frac{\partial T_s}{\partial t} = \frac{\partial}{\partial Z}\left(\lambda\frac{\partial T_s}{\partial Z}\right) \quad (10)$$

$$\frac{\partial \eta}{\partial t} = \frac{\partial}{\partial Z}\left(D_\eta\frac{\partial \eta}{\partial Z}\right) + \frac{\partial K_\eta}{\partial Z}, \quad (11)$$

where the hydraulic conductivity $K_\eta$ and diffusivity $D_\eta$ are functions of the soil moisture:

$$K_\eta = K_{\eta_s}\left(\frac{\eta}{\eta_s}\right)^{2b+3} \quad (12)$$

$$D_\eta = -\frac{bK_{\eta_s}\psi_s}{\eta}\left(\frac{\eta}{\eta_s}\right)^{b+3}. \quad (13)$$

In the above equations, $\eta_s$, $K_{\eta_s}$, and $\psi_s$ are the saturated values of volumetric water content, hydraulic conductivity, and moisture potential. Those parameters, the specific heat capacity $\rho c$ and the exponent $b$ are functions of the soil texture. The thermal conductivity $\lambda$ is also determined by the soil moisture:

$$\lambda = 0.167\eta + 0.1. \quad (14)$$

Based on Deardorff (1978), the surface scheme also allows for the inclusion of a single layer of vegetation, which is assumed to have negligible heat capacity. A second energy budget is established for the foliage layer, taking into account the exchanges above and below the canopy. In the present model, the leaf stomatal resistance is calculated as

$$r_{st} = r_{st_{min}}S_{st}M_{st}, \quad (15)$$

where $r_{st_{min}}$ is the minimum stomatal resistance (and is a function of the vegetation type), $S_{st}$ is the solar radiation factor, and $M_{st}$ is a factor limiting the transpiration when the soil becomes very dry or when the atmospheric demand is too strong (Pinty et al. 1989).

The necessary solar and infrared fluxes calculations at the ground are based on Mahrer and Pielke (1977). Scattering and absorption of solar radiation by permanent gases such as oxygen, ozone, and carbon dioxide is included. Absorption and longwave emission by the atmospheric water constituents (water vapor and clouds) is also considered. The surface radiative fluxes are modified to account for the terrain slope.

## 3. Initial conditions and model parameters

A set of four experiments was carried out to study the influence of vegetation on the development and structure of the mountain wave, as well as on the distribution in time and space of surface parameters. The astronomical parameters for radiation calculations correspond to 21 March at a latitude of 40°N. The simulations begin at 0600 LST (just after sunrise) and continue until 1800 LST (just before sunset). The model domain is 500 km, with a horizontal grid length of 10 km. The time step is 10 s.

### a. The atmosphere

The model is initialized with a single radio sounding, providing horizontally uniform initial fields. The layer below 300 hPa has a lapse rate of 6 K km$^{-1}$, in which the temperature at zero elevation has a value of 280 K and the layer between 300 hPa and the upper boundary (100 hPa) is isothermal. The wind is westerly with a vertically uniform speed of 20 m s$^{-1}$. Initially, the microphysical variables and all the surface fluxes are set to zero. Except for air moisture and surface characteristics, all the simulations are initialized in the same manner.

There are 15 vertical levels resulting in four computational levels in the lowest kilometer. The absorbing

TABLE 1. Mixed soil characteristics.

| Parameter | Value |
|---|---|
| Porosity | 0.458 |
| Saturated hydraulic conductivity ($10^{-6}$ m s$^{-1}$) | 5.65 |
| Saturated moisture potential (m) | −0.548 |
| Dry volumetric heat capacity ($10^6$ J m$^{-3}$ K$^{-1}$) | 1.242 |
| Exponent $b$ | 6.58 |
| Emissivity | 0.99 |
| Albedo | 0.14 |
| Roughness length (m) | 0.005 |

layer occupies the 5 upper levels of the domain, and the maximum diffusion induced at the top level has a nondimensional value of 0.10.

The lateral boundary conditions are specified using the relaxation method of Davies (1976). All the fields are relaxed toward their initial values as has been done in previous works (e.g., Richard et al. 1989).

### b. *The surface*

The orography consists of a north–south-oriented ridge, centered in the domain and defined by the function (Laprise and Peltier 1989)

$$z_s(x) = h\left[1 + \left(\frac{x}{a}\right)^2\right]^{-1},$$

where $h$ and $a$ are 1 and 20 km, respectively. The soil, with a depth of 1 m, is divided into 13 vertical levels. A mixed soil type is used for all simulations. Its hydraulic, thermal, and radiative properties are summarized in Table 1. For cases in which vegetation is included, two representative types of cover are considered, conifer forest and shrub. Their characteristics are listed in Table 2.

The experimental conditions are summarized in Table 3. Experiments 1 and 2 are carried out for bare soil but for different initial conditions of atmospheric moisture (dry atmosphere in experiment 1 and a saturated atmosphere in experiment 2), and are included for comparison with previous studies in which the surface energy budget was not used to calculate the surface temperature (Nickerson et al. 1986).

In experiments 3 and 4, both with saturated atmosphere, the surface is covered by vegetation. Two distinct vegetative regions are considered: the top [$z_s(x) \geq 500$ m] and the slopes [$z_s(x) < 500$ m]. The shielding factor is homogeneous over each vegetation area.

For each of the four experiments, the temperature of the atmospheric sounding at the air–land interface was used to initialize the vertically uniform temperature within the soil. The volumetric water content of the soil was initially 60% of the saturated value.

## 4. Results and discussion

It is not the aim of this paper to study the effects of soil moisture and texture. Therefore, all the simulations presented in this work have been performed with the same soil properties.

TABLE 2. Specification of vegetative characteristics in experiments 3 and 4.

| Parameter | Conifer forest | Shrub |
|---|---|---|
| Height (m) | 20.0 | 0.5 |
| Displacement height (m) | 15.0 | 0.37 |
| Plant resistance (s) | $8 \times 10^9$ | $10 \times 10^9$ |
| Minimum stomatal resistance (s m$^{-1}$) | 350 | 500 |
| Critical leaf water potential (m) | −150 | −150 |
| Green leaf area index | 3.5 | 1.0 |
| Dry leaf area index | 0.7 | 2.0 |
| Rooting depth (m) | 0.8 | 0.4 |
| Emissivity | 0.98 | 0.98 |
| Albedo | 0.10 | 0.16 |
| Roughness length (m) | 1.67 | 0.04 |

### a. *Wave structure*

The cross sections presented correspond to the central part of the model domain. Two representative times are considered when discussing the results given by the model, 1200 and 1800 LST.

Figure 1 displays the wave obtained for experiment 1. The maximum amplitude of the potential temperature wave develops at an altitude between 6 and 8 km over the lee of the ridge, and enhanced surface winds also appear in the lee. These results are qualitatively and quantitatively in agreement with previous experiments (Mahrer and Pielke 1978; Nickerson et al. 1986). However, in contrast to the conditions considered by Nickerson et al. (1986), the surface temperature in our simulations is allowed to vary, thereby resulting in some differences, especially in the lower part of the atmosphere. The development of thermally induced slope winds could explain, for example, why in our experiment the west slope surface winds are stronger and the east slope winds weaker.

From Figs. 1a and 1b, it can also be seen how the wave intensity decreases during the simulation. Without additional information, it is difficult to assess to what extent

TABLE 3. Summary of the numerical experiments.

| Experiment | Atmosphere | Zone | Vegetation type | Shielding factor |
|---|---|---|---|---|
| 1 | Dry | Top | — | — |
| | | Slopes | — | — |
| 2 | Saturated | Top | — | — |
| | | Slopes | — | — |
| 3 | Saturated | Top | Conifer forest | 0.9 |
| | | Slopes | Shrub | 0.8 |
| 4 | Saturated | Top | Shrub | 0.8 |
| | | Slopes | Shrub | 0.8 |

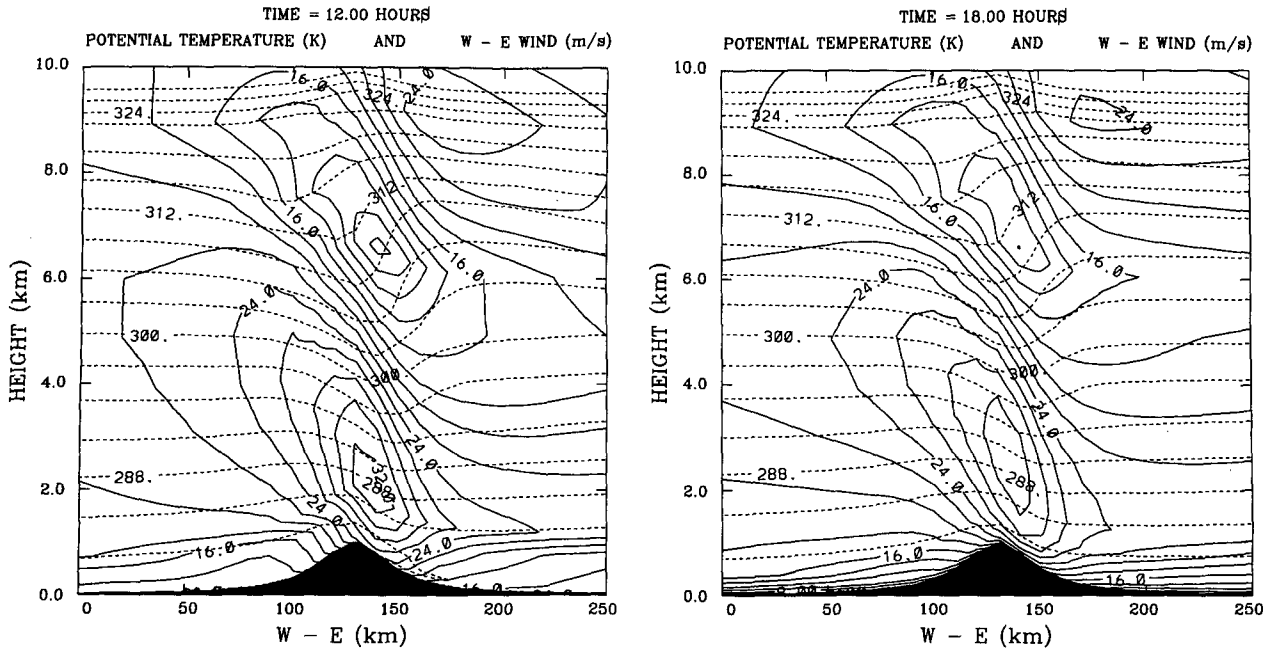


FIG. 1. Vertical cross section showing zonal horizontal velocity (solid line) and potential temperature (dashed line) for experiment 1: (a) 1200 LST, (b) 1800 LST.

this result is a consequence of the diurnal variability in the boundary layer or if it is due to a spinup process within the model. This point will be discussed in section 4e.

The saturated case (experiment 2) after 12 h of simulation is presented in Fig. 2a. In agreement with Durran and Klemp (1983), the figure shows that the inclusion of moisture produces a weaker wave than is obtained in the dry case. Comparing the result with Fig. 1b, it can be also seen that the inclination of the wave is smaller when moisture is present.

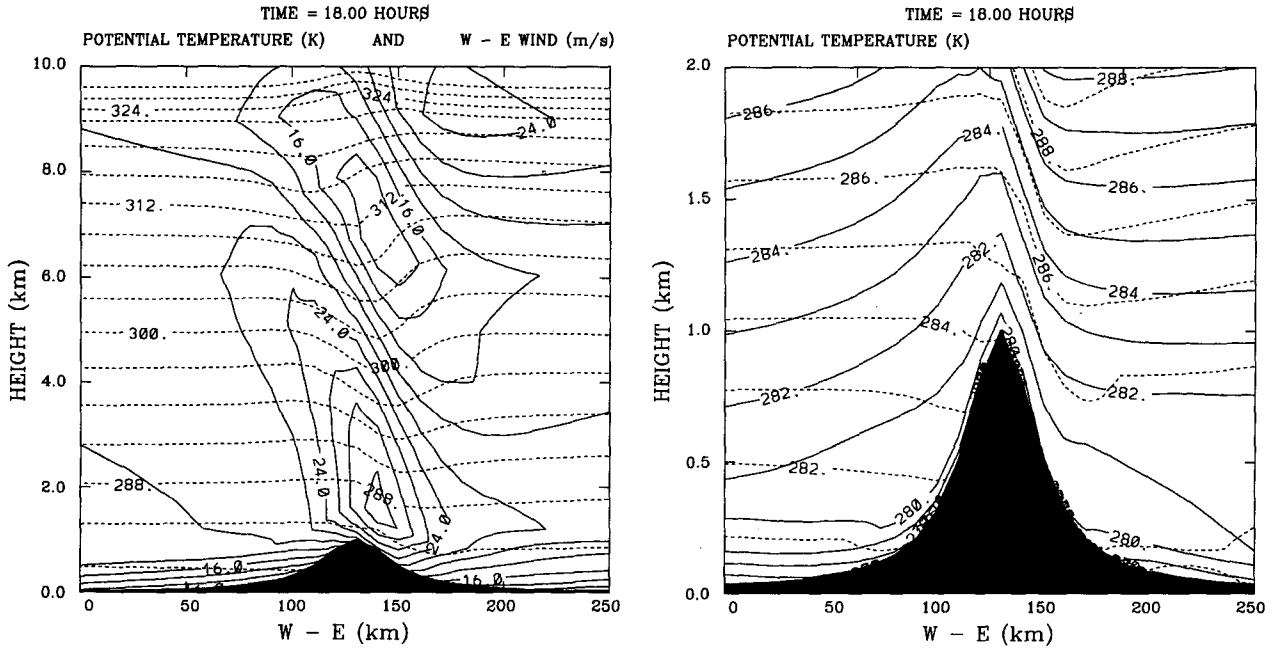


FIG. 2. (a) As in Fig. 1 but for experiment 2 at 1800 LST. (b) Detailed view of potential temperature around the mountain for experiments 1 (solid line) and 2 (dashed line) at 1800 LST.

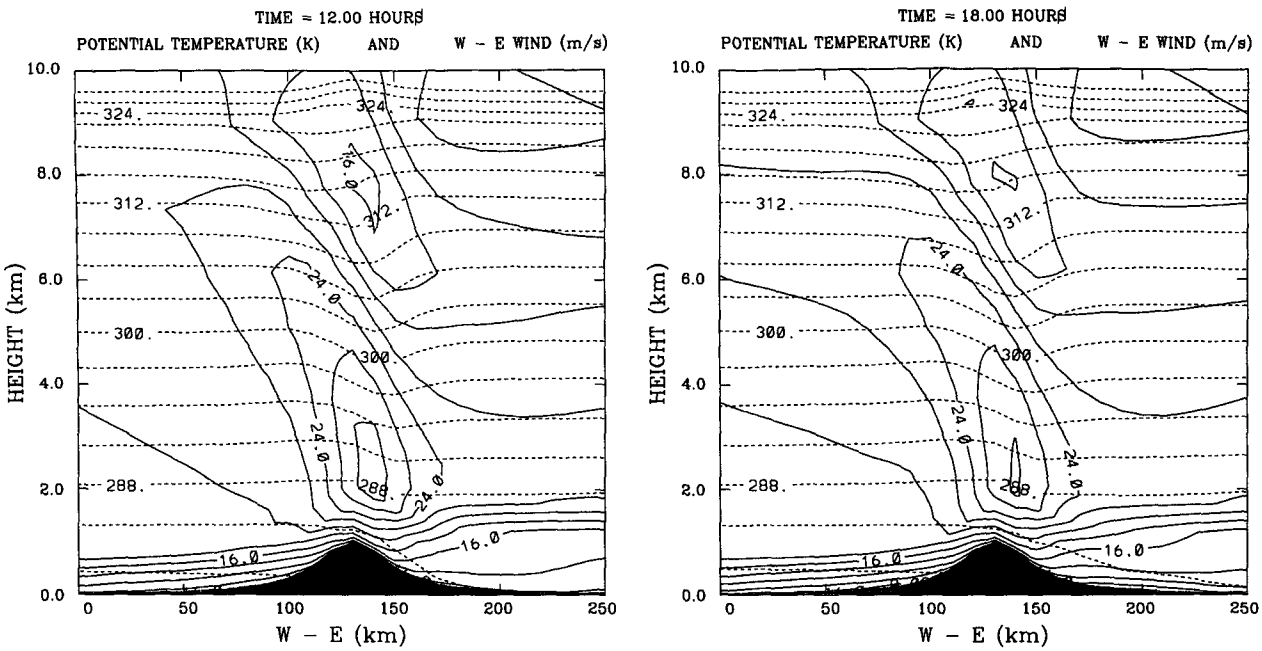


FIG. 3. As in Fig. 1 but for experiment 3: (a) 1200 LST, (b) 1800 LST.

Another moisture effect derived from the heat released by the condensation products in the ascending slope is the additional warming in the lee (foehn effect). This moisture effect is detected from a comparison of Figs. 1b and 2a (see Fig. 2b for a detailed view). The same comparison shows that the lower atmosphere is warmer over the whole domain and less stable in the lee for the saturated case. This reduction of stability in the moist case was also present in the simulations of Nickerson et al. (1986).

Having established the validity of our results by comparison with previous works, two more experiments were carried out to study the effects of surface vegetation on the wave structure. Figures 3 and 4 display the results for experiment 3 (nonhomogeneous vegetation) and experiment 4 (homogeneous vegetation).

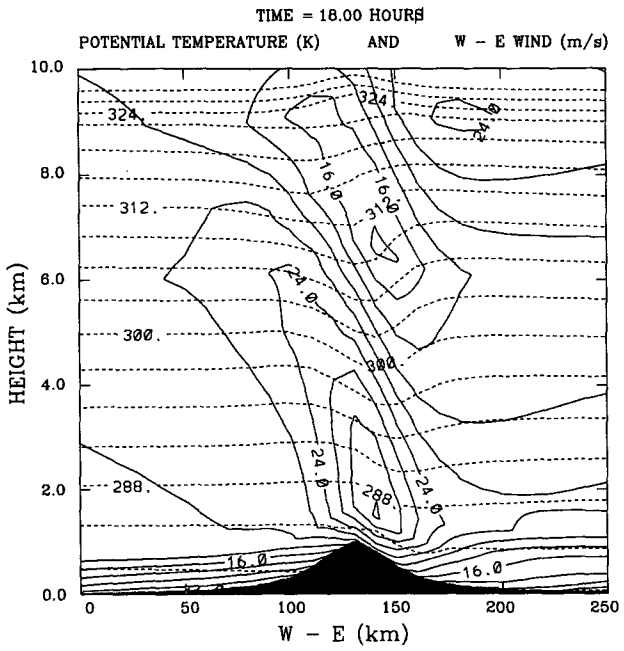


FIG. 4. As in Fig. 1 but for experiment 4 at 1800 LST.

The wave obtained in case 3 (Fig. 3) is appreciably weaker than the wave with bare soil. The centers of maximum and minimum winds are situated 1 km higher in this case, and the midtropospheric amplitude of the temperature wave is not as pronounced. Over the crest of the ridge, where friction induced by conifers is very intense, the wind shear extends vertically to higher altitudes than in experiment 2. At low levels, isotachs are more symmetrically distributed between both slopes in Fig. 3 than in Fig. 2a, indicating that a dense stand of tall trees at the crest of the mountain may significantly reduce the intensity of downslope winds. In this case, the wave intensity is also stronger at 1200 LST than at 1800 LST.

There is a region of reduced stability in the lower atmosphere over the eastern slope of the barrier at noon (Fig. 3a). Over that same area, the stratification becomes more stable by 1800 LST (Fig. 3b), but does not reach the degree of stability found over the western slope. Of all three saturated experiments, the reduction

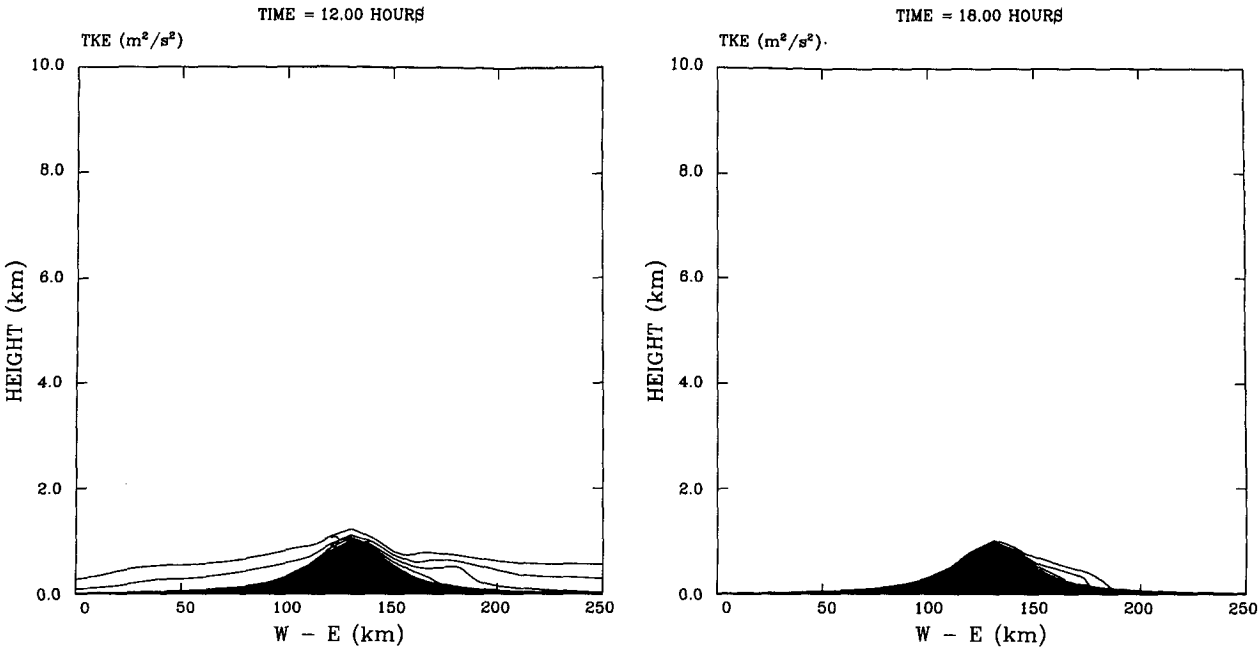


FIG. 5. Vertical cross section of the turbulent kinetic energy field for experiment 1: (a) 1200 LST, (b) 1800 LST. The contours are drawn every 0.5 $m^2 s^{-2}$ starting at 0.5 $m^2 s^{-2}$.

in leeside stability is most pronounced in experiment 3.

As expected, when the tall trees at the top of the mountain are replaced by shrub, the wave intensity given by the model (Fig. 4) evolves to an intermediate state between the results of experiments 2 and 3. The reduced surface friction associated with the uniform covering of shrub on the slopes as well as on the crest of the mountain results in leeside surface winds that are 4 m $s^{-1}$ stronger than when the crest is covered by tall trees.

### *b. Turbulent kinetic energy*

An important aspect of the dynamical and thermodynamical fields induced by the mountain is the intensity and distribution of the turbulent kinetic energy. Figures 5–8 display the TKE obtained in the experiments, as well as the areas affected by clouds. (No clouds are formed in case 1 since the moist soil is not a significant source of moisture for the atmosphere.) In the prognostic equation of TKE [eq. (9)], in addition to the transport terms, there are three important terms that maintain a near balance in the free atmosphere, resulting in no net turbulence production. These are the shear production, the buoyancy production (negative in stable conditions), and the viscous dissipation. Wherever the stratification is sufficiently stable, even with appreciable wind shear, no turbulence appears. However, since in our experiments the stability of the PBL reaches low values, especially in the lee for the saturated cases as a result of the foehn effect, and since there are regions of strong wind shear close to the slopes, this leads to the generation of turbulence at low levels, primarily above the lee slope.

The TKE figures show that the turbulence is stronger at noon when the PBL is less stable than in the evening in all cases. However, the four simulations result in significant differences in the TKE intensity and distribution. We note in Figs. 5–8 that the dry case is not as favorable for turbulence production as the moist cases in spite of having stronger wind shear. This is because the midday reduction of the thermal stability only affects a very shallow layer close to the ground where the temperature increases markedly in response to the incoming solar radiation. In fact, the turbulence distribution in this case is very homogeneous along the domain at noon (Fig. 5a) since the increase of the surface temperature is nearly the same over the whole domain. Since the longwave radiation is not readily absorbed by the dry atmosphere, the surface cools rapidly during the afternoon, and by the end of the simulation, turbulence has practically disappeared except over the eastern slope where the wind shear is stronger (Fig. 5b).

In the saturated cases (Figs. 6–8), the solar radiation is appreciably absorbed and the ground temperature cannot increase as much as will be seen in section 4d. By way of contrast, downwind of the barrier the lower atmosphere remains slightly stable owing to the foehn warming effect. As a result, the turbulence distribution is highly skewed, with low values upwind of the barrier and high values downwind associated with the wind shear and light stability within the PBL.

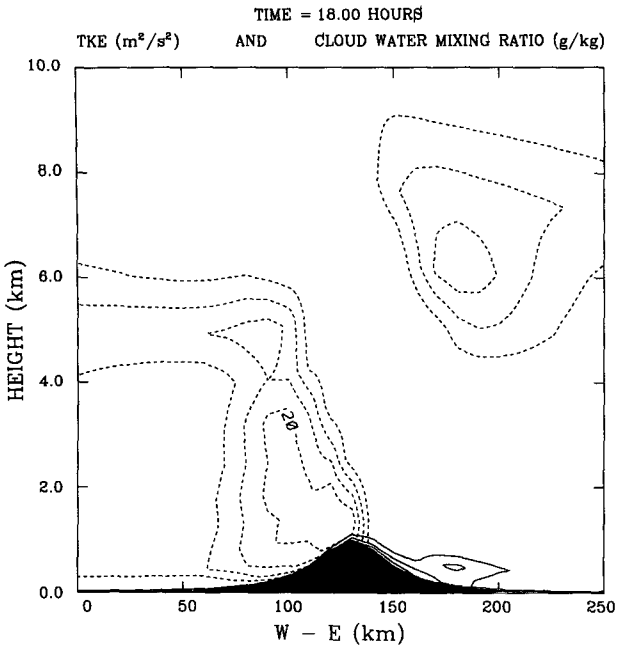


FIG. 6. Vertical cross section of the turbulent kinetic energy field (solid line) and cloud water mixing ratio (dashed line) for experiment 2 at 1800 LST. The solid contours are drawn every 0.5 $m^2 s^{-2}$ starting at 0.5 $m^2 s^{-2}$. The dashed contours are drawn every 0.05 g $kg^{-1}$ starting at 0.05 g $kg^{-1}$.

It is important to note the role played by the conifer forest, through its extensive layer of wind shear, in the formation of a deep and intense turbulent layer (Fig. 7). That layer has a depth of 1 km in the lee of the mountain, but it also exists in a shallow layer above the western slope. The results for experiments 2 and 4 (Figs. 6 and 8) are similar since there are only minor differences of wind and temperature at low levels. In these cases, the region of turbulence is found in a shallow layer over the eastern slope.

### c. *Clouds and precipitation*

The cloud water mixing ratio for the cases that were initially saturated is shown in Figs. 6, 7, and 8. The clouds induced by orographic uplifting over the upwind slope are present in all three experiments. The greatest vertical extent is observed for the case when the conifer forest covers the top of the mountain. The maximum values of the liquid water content are also obtained for this case (more than 0.25 g $kg^{-1}$ close to the crest). The major differences between the three experiments upwind of the barrier is the strength of the cloud band at an altitude of 4 and 6 km. Cases 3 and 2 produce the highest and lowest liquid water concentrations, respectively. Case 4 again produces intermediate values.

In addition, the vertical motion induced by the wave downwind of the barrier leads to the formation of a cloud with low liquid water content at an altitude between 6 and 8 km. Experiment 3 has the lowest liquid water content in that upper-level cloud owing to a weaker intensity of the upper-level wave. More condensation occurs in the upper-level cloud of experiment 4 (Fig. 8), but the greatest amount is produced in experiment 2 (Fig. 6).

Model-predicted accumulated rainfall over the mountain barrier is shown in Fig. 9. The asymmetrical distribution of cloud water results in heavier rainfall over the upwind slope and crest, with an abrupt decrease over the lee of the ridge. In the proximity of the eastern boundary, a secondary maxima appears as a consequence of the upper cloud formation, but only for experiments 2 and 4.

The amount of rainfall given by the model is sensitive to the surface vegetative cover. The amount of precipitation reaching the surface of the western slope is enhanced when the soil is covered by shrub, while the case with the conifer forest covering the crest of the ridge produces the most rainfall over both slopes.

### d. *Surface parameters*

Figures 10–12 show the temporal evolution of surface parameters at three locations on the mountain barrier: one at the top of the ridge (TOP), and two others at an elevation of 200 m (EAST and WEST). It should be noted that atmospheric and subsurface soil models are fully coupled and interactive. Near-ground gradients of temperature and moisture depend not only on the evolving structure of the atmospheric wave but also on other factors such as rain, which is absorbed by the soil and accumulated on the leaves of the surface vegetation.

Figure 10 shows the diurnal curves of net radiation at the surface for the saturated cases. The curves for the dry case (not shown) revealed that there is net loss during the beginning and ending stages of the simulation in which the sun angle is still low, but high positive values occur during the central part of the day (up to 550 W $m^{-2}$ at noon) when the solar radiation reaches the ground without significant atmospheric absorption.

However, as can be seen in Fig. 10, significant radiative loss does not occur in the saturated cases owing to the downward longwave reemission by atmospheric water vapor. On the other hand, the atmospheric water constituents (vapor and liquid water) exert an important attenuation of the solar radiation, and the net radiation at the surface is therefore reduced.

The liquid water of clouds is a major factor in determining the amount of solar radiation reaching the ground. The diurnal curves for the three experiments at sites covered by dense clouds (WEST and TOP) are nearly identical, although higher values are obtained over the top where there is less cloud water in the column of air above the summit. However, over the eastern slope the net radiative energy for case 3 differs ap-

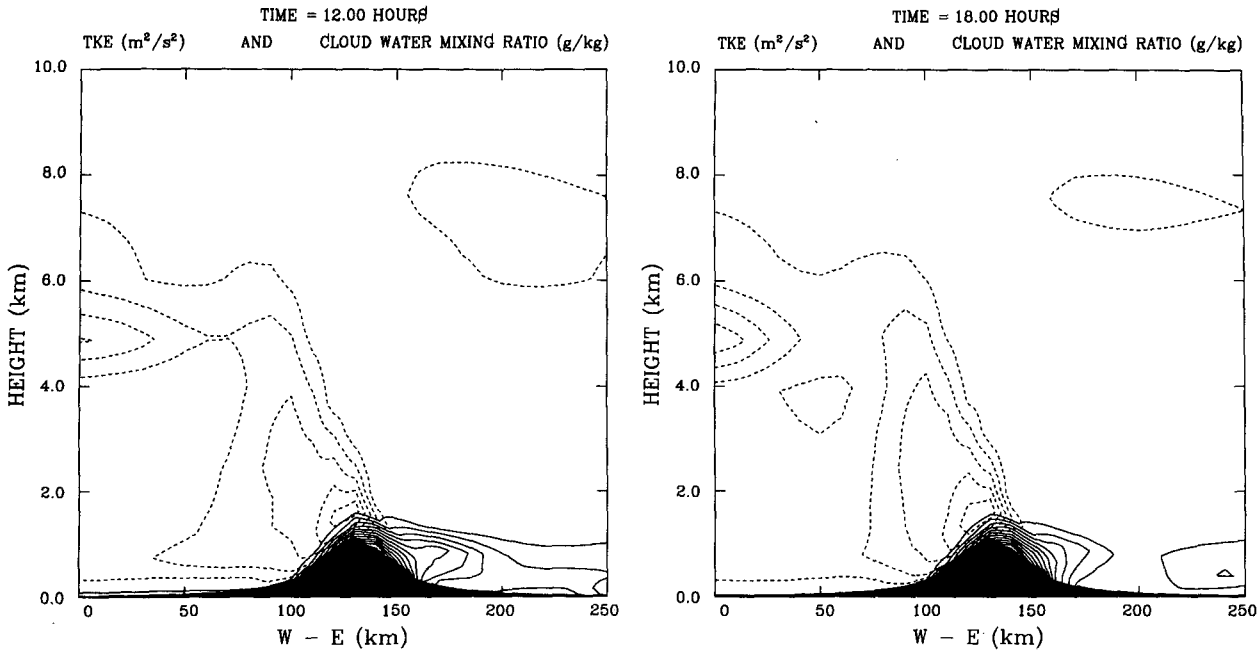


FIG. 7. As in Fig. 6 but for experiment 3: (a) 1200 LST, (b) 1800 LST.

preciably from the values obtained for cases 2 and 4. As noted in the previous section, the cloud generated by the mountain wave downwind of the barrier is not as well developed in case 3, and the net radiation at the surface exceeds that obtained for cases 2 and 4 by 100 W $m^{-2}$ at noon.

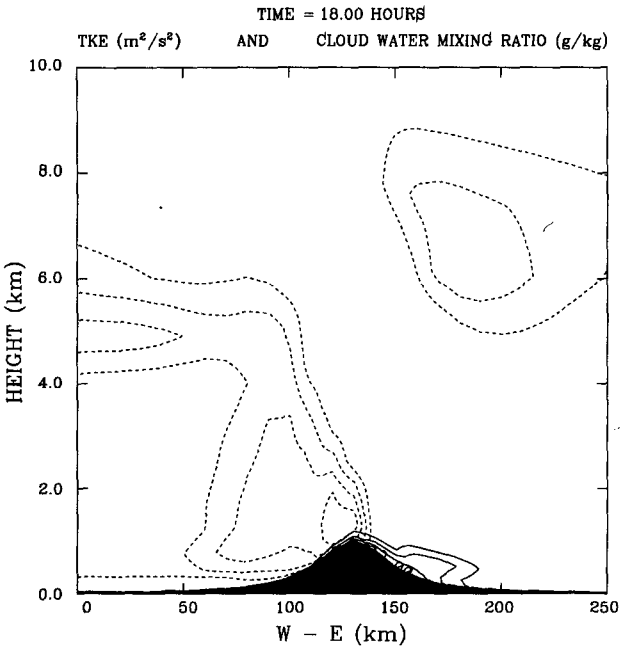


FIG. 8. As in Fig. 6 but for experiment 4 at 1800 LST.

The uniformity in net radiation previously noted also applies to the ground temperatures for the TOP and WEST locations, except that the case with bare soil yields slightly higher temperatures (Fig. 11). The effect of vegetation is to reduce the thermal oscillation during midday, since part of the incoming radiation is consumed by vegetative processes. For all cases, the daytime temperature increase for those locations is less than 1.5 K. For the EAST location where the solar radiation arrives less attenuated, the daytime increase exceeds 2 K, but the curves are more complex owing to the absorption of the enhanced incoming solar radiation by the vegetative surface.

Figure 12 shows that at the height of 15 m, corresponding to the first computational level of the atmospheric model, the temperature is nearly identical for the three simulations. The maximum temperatures are reached at 1300 LST, but there is a significant difference between the values on the eastern and western slopes, with the air over the eastern slope being warmer by 3 K. This fact reflects the wave-induced heating associated with the foehn effect.

Another important aspect is the energy partition between the transpiration (latent heat flux) and the sensible heat fluxes in areas covered by vegetation. This partition is controlled primarily by the leaf stomatal resistance (Pinty et al. 1989). Figures 13 and 14 show the temporal variation of both fluxes for a conifer forest and for the case of shrub covering the top of the ridge. The result is consistent with their different minimum stomatal resistances given in Table 2. Since the stomatal resistance is larger for shrubs than for conifer trees, the

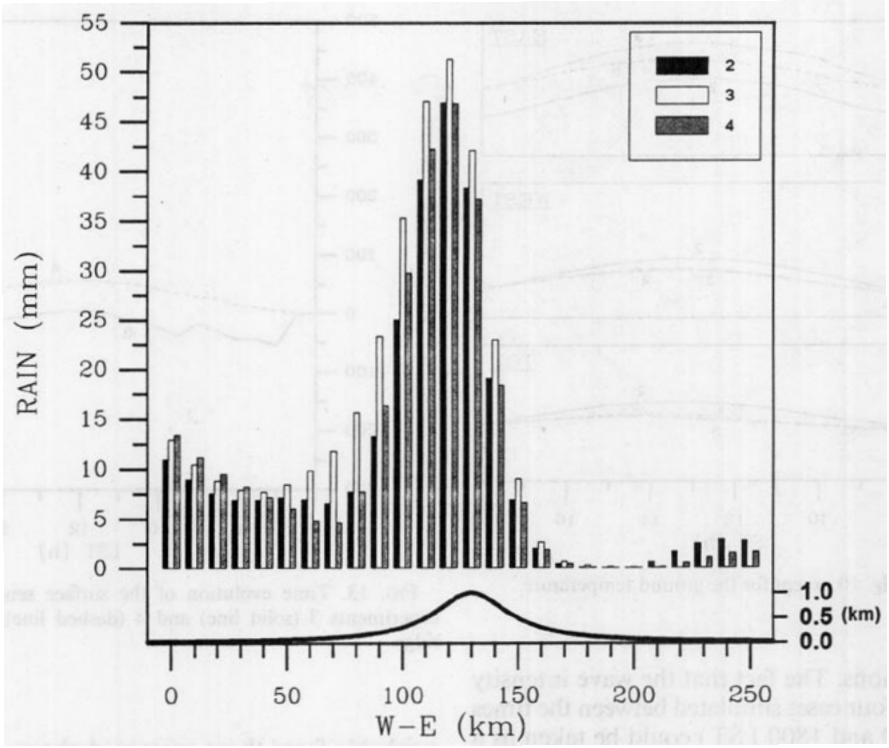


FIG. 9. Model-predicted rainfall after the period of simulation for experiments 2, 3, and 4 (black, white, and gray bars, respectively).

transpiration for the shrub-covered surface is lesser, resulting in a smaller latent heat flux. On the other hand, the sensible heat flux is greater for shrubs than for conifer trees.

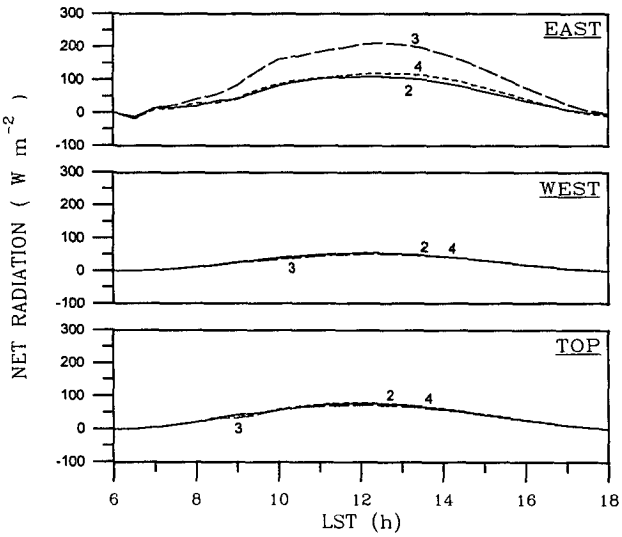


FIG. 10. Time evolution of the net radiation at the surface for experiments 2 (solid line), 3 (long dashes), and 4 (short dashes) in the top of the ridge (TOP), at an elevation of 200 m on the west slope (WEST), in the symmetric point on the east slope (EAST).

*e. Drag and model adjustment*

A measure of the strength of the wave response is the surface pressure drag across the ridge. This is defined by

$$D = \int_0^L \pi \frac{\partial z_s}{\partial x}\, dx,$$

where $L$ is the length of the domain. The time-dependent development of the pressure drag for the different experiments is shown in Fig. 15. After a period of adjustment, the four simulated mountain waves reach a nearly stationary state before the end of the simulations. The drag value that is ultimately reached in the dry case ($0.16 \times 10^6$ kg s$^{-2}$) is practically the same as in the moist cases, even though the tendencies prior to 1200 LST are different. A possible explanation for that result could be the foehn effect previously mentioned. Although the difference of pressures between both sides of the ridge induced by the wave itself is larger for a dry atmosphere, there is at the same time in the moist cases another mechanism that tends to accentuate that difference by lowering the pressure above the lee slope. That air is warmer and less dense and therefore serves to compensate for the stronger dynamic effect of the dry wave.

An important consideration in the assessment of the results is the time required for the model to adjust to

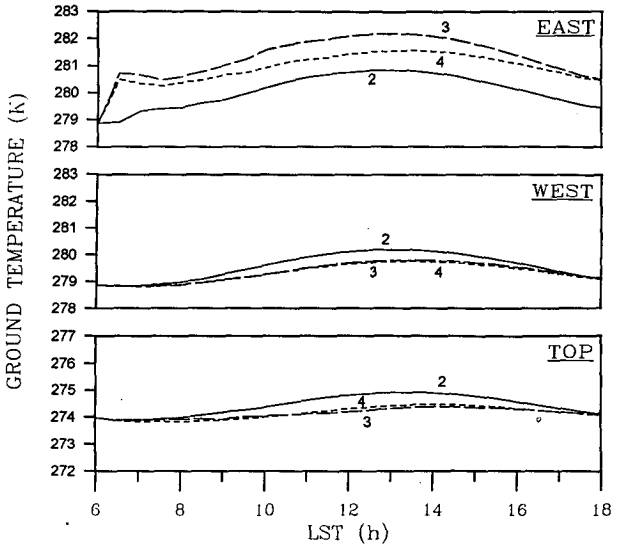


FIG. 11. As in Fig. 10 except for the ground temperature.

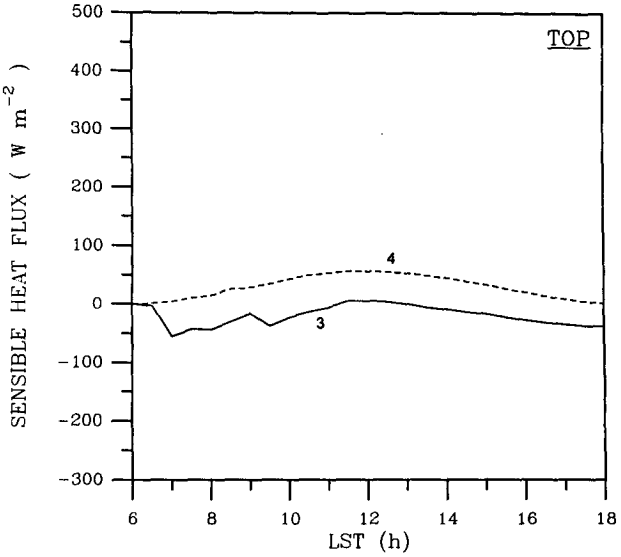


FIG. 13. Time evolution of the surface sensible heat flux for experiments 3 (solid line) and 4 (dashed line) at the top of the ridge.

the initial conditions. The fact that the wave intensity decreases for the four cases simulated between the times considered (1200 and 1800 LST) could be taken as a consequence of the model adjustment. However, the adjustment of the surface drag to near equilibrium values in only 1 h suggests that the spinup process does not significantly affect the results. That initial assessment was subsequently confirmed by carrying out experiment 3 for a period of 48 h. The fields for the second day of simulation (not shown) are nearly indistinguishable from those presented above, indicating that the temporal evolution of the fields represents the effects of temporal changes in the boundary layer rather than a model adjustment process. That conclusion is confirmed in Fig. 16, which presents the surface drag for that period of 48 h. The uniformity of the drag after 1800 LST indicates that the model has completely adjusted. The appearance of a slight dome in the curve on the second day is attributed to a new strengthening of the wave.

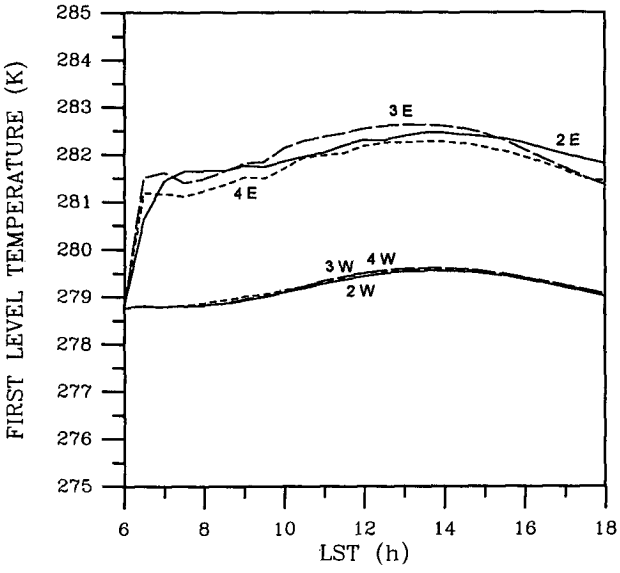


FIG. 12. Time evolution of the air temperature given by the model at the first computational level (15 m above the ground approximately) over both slopes, for experiments 2 (solid line), 3 (long dashes), and 4 (short dashes): E and W refer to the east and west slope, respectively.

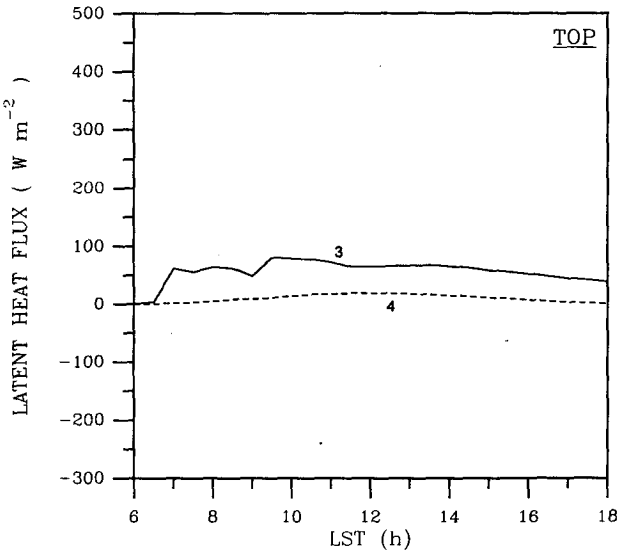


FIG. 14. As in Fig. 13 except for the latent heat flux.

## 5. Conclusions

A two-dimensional meso-$\beta$ model with a coupled soil and vegetation submodel has been used to study the effects of different vegetative surfaces on orographically generated atmospheric waves. In the absence of vegetation but with a moist soil, the atmospheric wave structure for both dry and saturated atmosphere is in good agreement with previous studies (Nickerson et al. 1986) but shows a redistribution of winds at low levels owing to a more realistic treatment of the ground temperature that is allowed to vary in response to the evolving surface energy fluxes.

The inclusion of dense vegetation in the simulation of mountain waves reveals a great sensitivity of the airflow and thermal structure at all levels of the model to the treatment of the lower boundary. A tall, dense, vegetative surface such as a conifer forest significantly diminishes the intensity of the mountain wave. As a result of a higher symmetry of isotachs between both slopes at low levels, this case corresponds to a diminution of the stronger downslope surface winds and the creation of an extensive layer of vertical wind shear in the proximity of the summit. That deep layer of strong wind shear in the low atmosphere, combined with low stability, seems to be an important agent in the development of turbulence. The reduction in atmospheric stability associated with foehn conditions in a moist environment has important consequences for the development of turbulence downwind of a mountain barrier.

The model-predicted rainfall suggests an important role for vegetation in the development of clouds and the enhancement of precipitation. When the surface is covered by shrub, enhanced rainfall occurs from the orographic cloud that develops over the upwind slope. But when the shrub on the crest of the mountain is replaced by a conifer forest as typically occurs in many parts of the world, the rainfall over the upwind and downwind slopes is enhanced.

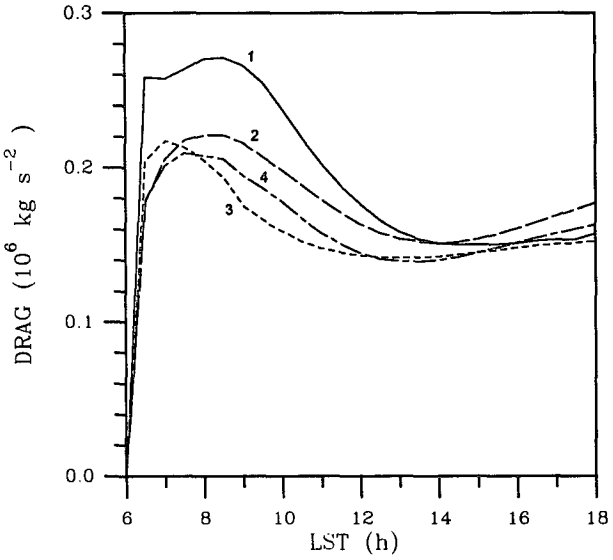


FIG. 15. Time evolution of the surface pressure drag across the ridge for experiments 1 (solid line), 2 (long dashes), 3 (short dashes), and 4 (long and short dashes).

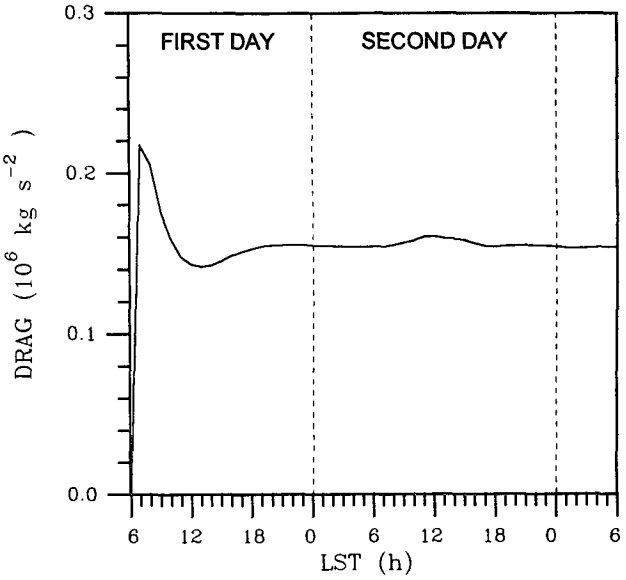


FIG. 16. Time evolution of the surface pressure drag for a simulation of 48 h for experiment 3.

The results obtained in this work show the importance of surface-induced frictional effects on the simulation of surface airflow, stability, and turbulent kinetic energy of orographically forced circulations. Improved simulations and model predictions of airflow over mountainous terrain will require an adequate treatment of the vegetative canopy in the surface energy budget calculation. These findings may be particularly relevant to studies of atmospheric dispersion in the PBL over complex vegetative surfaces.

*Acknowledgments.* This work has been partially supported by DGICYT PB89-0428 grant.

## APPENDIX

### List of Symbols

| | |
|---|---|
| $a$ | half-width of the ridge |
| $B$ | vertical scale factor |
| $C_p$ | specific heat at constant pressure |
| $C_\epsilon$ | numerical coefficient for the TKE dissipation term |
| $D_{\pi u}$, $D_S$, $D_W$, $D_{\pi q_r}$, $D_{\pi N_r}$, $D_{\pi e}$ | horizontal diffusion terms |
| $e$ | turbulent kinetic energy |
| $F_{\pi u}$, $F_S$, $F_W$, $F_{\pi q_r}$, $F_{\pi N_r}$, $F_{\pi e}$ | turbulent mixing terms |

| | |
|---|---|
| $g$ | acceleration of gravity |
| $h$ | maximum height of the ridge |
| $H$ | entropy |
| $K_m$, $K_\theta$, $K_e$ | exchange coefficients |
| $l_k$ | mixing length scale |
| $l_\epsilon$ | dissipation length scale |
| $L_v$ | latent heat |
| $N_r$ | raindrop number concentration |
| $P$ | pressure |
| $P_0$ | reference pressure (1000 hPa) |
| $P_s$ | surface pressure |
| $P_t$ | pressure at the upper boundary (100 hPa) |
| $\hat{P}$ | $\left(\frac{P}{P_0}\right)^{R_v/C_p}$ |
| $q_{cw}$ | cloud water mixing ratio |
| $q_r$ | rainwater mixing ratio |
| $q_v$ | water vapor mixing ratio |
| $R_v$ | universal gas constant |
| $S$ | entropy variable defined by $S = \pi H$ |
| $S_S$, $S_W$, $S_{\pi q_r}$, $S_{\pi N_r}$ | source–sink terms |
| $t$ | time |
| $T^*$ | virtual temperature |
| $u$ | wind component along the $x$ coordinate |
| $W$ | moisture variable defined by $W = \pi(q_v + q_{cw})$ |
| $x$ | coordinate in the west–east direction |
| $z_s$ | surface height |
| $\gamma_{cg}$ | temperature countergradient |
| $\pi$ | $P_s - P_t$ |
| $\sigma$ | pressure coordinate defined by $\sigma = (P - P_t)/\pi$ |
| $\sigma'$ | $d\sigma/d\nu$ |
| $\nu$ | vertical coordinate related to $\sigma$ by $\sigma = (4\nu - \nu^4)/3$ |
| $\dot{\nu}$ | vertical velocity |
| $\phi$ | geopotential |
| $\theta$ | potential temperature |
| $\theta_v$ | virtual potential temperature, $\theta_v = \theta(1 + 0.61q_v)$ |

## REFERENCES


Anthes, R. A., and T. T. Warner, 1978: Development of hydrodynamic models suitable for air pollution and other mesometeorological studies. *Mon. Wea. Rev.*, **106,** 1045–1078.

Bougeault, P., and P. Lacarrère, 1989: Parameterization of orography induced turbulence in a mesobeta-scale model. *Mon. Wea. Rev.*, **117,** 1872–1890.

Davies, H. C., 1976: A lateral boundary formulation for multi-level prediction models. *Quart. J. Roy. Meteor. Soc.*, **102,** 405–418.

Deardorff, J. W., 1978: Efficient prediction of ground surface temperature and moisture, with inclusion of a layer of vegetation. *J. Geophys. Res.*, **83,** 1889–1903.

Durran, D. R., and J. B. Klemp, 1983: A compressible model for the simulation of moist mountain waves. *Mon. Wea. Rev.*, **111,** 2341–2361.

Klemp, J. B., and D. K. Lilly, 1978: Numerical simulation of hydrostatic mountain waves. *J. Atmos. Sci.*, **35,** 78–107.

Laprise, R., and W. R. Peltier, 1989: On the structural characteristics of steady finite-amplitude mountain waves over bell-shaped topography. *J. Atmos. Sci.*, **46,** 586–595.

Mahfouf, J. F., E. Richard, and P. Mascart, 1987: The influence of soil and vegetation on the development of mesoscale circulations. *J. Climate Appl. Meteor.*, **26,** 1483–1495.

Mahrer, Y., and R. A. Pielke, 1977: The effects of topography on the sea and land breezes in a two-dimensional numerical model. *Mon. Wea. Rev.*, **105,** 1151–1162.

——, and ——, 1978: A test of an upstream spline interpolation technique for the advective terms in a numerical mesoscale model. *Mon. Wea. Rev.*, **106,** 818–830.

McCumber, M. C., and R. A. Pielke, 1981: Simulation of the effects of surface fluxes of heat and moisture in a mesoscale numerical model. 1. Soil layer. *J. Geophys. Res.*, **86,** 9929–9938.

Nickerson, E. C., and E. L. Magaziner, 1976: A three-dimensional simulation of winds and non-precipitating orographic clouds over Hawaii. NOAA Tech. Rep. ERL 377-APCL 39.

——, E. Richard, R. Rosset, and D. R. Smith, 1986: The numerical simulation of clouds, rain and airflow over the Vosges and Black Forest mountain: A meso-$\beta$ model with parameterized microphysics. *Mon. Wea. Rev.*, **114,** 398–414.

Pinty, J. P., P. Mascart, E. Richard, and R. Rosset, 1989: An investigation of mesoscale flows induced by vegetation inhomogeneities using an evapotranspiration model calibrated against HAPEX-MOBILHY data. *J. Appl. Meteor.*, **28,** 976–992.

Richard, E., P. Mascart, and E. C. Nickerson, 1989: The role of surface friction in downslope windstorms. *J. Appl. Meteor.*, **28,** 241–251.

Schlesinger, R. F., L. W. Uccellini, and D. R. Johnson, 1983: The effects of the Asselin time filter on numerical solutions to the linearized shallow-water wave equations. *Mon. Wea. Rev.*, **111,** 455–467.

Therry, G., and P. Lacarrère, 1983: Improving the eddy-kinetic energy model for planetary boundary layer description. *Bound.-Layer Meteor.*, **25,** 63–88.